Optics & Laser Technology 195 (2026) 114591

Contents lists available at ScienceDirect

Optics and Laser Technology

journal homepage: www.elsevier.com/locate/optlastec

Full length article

Exploring real-time monitoring of laser-induced recrystallization using acoustic emissions

Claire Navarre [a,1], William Hearn [b,1,**], Mathijs Van der Meer [a], Lucas Schlenger [a], Rik Vaerenberg [c,d], Nicolas Mari [a], Reza Esmaeilzadeh [a], Amir M. Jamili [a], Vigneashwara Pandiyan [e], Steven Van Petegem [b,*], Roland E. Logé [a]

[a] Thermomechanical Metallurgy Laboratory (LMTM) – PX Group Chair, École Polytechnique Fédérale de Lausanne (EPFL), CH-2002 Neuchâtel, Switzerland
[b] Structure and Mechanics of Advanced Materials, Laboratory for Condensed Matter, Center for Photon Science, Paul Scherrer Institute, Forschungsstrasse 111, 5232 Villigen, Switzerland
[c] Department of Mechanical Engineering, Division LMSD, KU Leuven, Celestijnenlaan 300, Box 2420, Leuven 3001, Belgium
[d] Flanders Make@KU Leuven, Leuven, Belgium
[e] Laboratory for Advanced Materials Processing, Empa- Swiss Federal Laboratories for Materials Science and Technology, 3602 Thun, Feuerwerkstrasse 39, Switzerland

ARTICLE INFO

Keywords:
Recrystallization
Acoustic emissions
In situ monitoring
X-ray diffraction
Laser processing
Heat treatment
Stainless steel

ABSTRACT

This study explores the use of acoustic emission (AE) signals for in situ characterization of recrystallization during laser processing. With millisecond-scale temporal resolution, AE monitoring can detect critical events during the recrystallization processes, including dislocation reorganization, nucleation, and grain growth. To connect such AE signals to recrystallization events, simultaneous in situ X-ray diffraction measurements were performed to establish a ground truth that could be correlated to collected AE data. From these experiments, a dominant frequency related to recrystallization was identified at ~ 188 kHz using the current experimental setup. This frequency was isolated by filtering the raw AE data via a combination of power spectrum density distribution analysis, harmonic identification, and empirical mode decomposition. Focusing on the AE data from this frequency, it was possible to identify critical events during recrystallization, including the onset of nucleation as well as the completion of the recrystallization process. These findings represent the first attempt to unveil the acoustic signature of recrystallization, demonstrating the potential for real-time monitoring and control of diffusive microstructural evolutions during rapid processing. They further suggest that AE monitoring can serve as a powerful tool to optimize laser processing and enable precise microstructure control during recrystallization.

1. Introduction

Recrystallization and associated annealing phenomena play a significant role in metals processing, as they enable the softening of deformed alloys as well as the refinement of microstructures by eliminating crystal defects and undesired crystallographic textures [1,2]. Recently, there has been growing interest in understanding recrystallization during rapid laser processing such as additive manufacturing [3–5], which involves heating and cooling over relatively short timescales and at high temperatures. Such rapid thermal changes during processing induce the formation of unique microstructures, that are not easy to achieve via conventional processing. However, it also makes it challenging to control the produced microstructure [6,7]. As such, it has been difficult to quantify as well as track the recrystallization behaviour of metals under such rapid conditions.

To date, numerous techniques have been used to quantify recrystallization in metals. One of the most prominent is electron back scattered diffraction (EBSD) which can characterize important microstructural characteristics (e.g., grain morphologies, sizes, crystallographic orientation, and misorientations) related to recrystallization [1,8]. Despite this, EBSD has limited spatial resolution when measuring on the nanometre scale and requires additional analysis via transmission

* Corresponding author.
** Corresponding author.
E-mail addresses: william.hearn@psi.ch (W. Hearn), steven.vanpetegem@psi.ch (S. Van Petegem).
[1] First authors.

https://doi.org/10.1016/j.optlastec.2025.114591
Received 25 August 2025; Received in revised form 7 December 2025; Accepted 25 December 2025
Available online 28 December 2025

electron microscopy (TEM) to achieve the required spatial resolution to study nanometric grains and severe plastic deformation [9,10]. EBSD and TEM are also destructive techniques that are conducted post-mortem, meaning they cannot capture the dynamic nature of recrystallization. Other alternatives, such as laboratory X-ray diffraction or neutron diffraction, use the peak-related features of the captured diffraction patterns to determine the crystallographic texture and grain size while also measuring the lattice distortions that arise from dislocations and stress fields [11,12]. While both techniques can follow the dynamics of slow recrystallization processes, it is difficult for them to capture the dynamic nature of recrystallization under rapid conditions.

Due to these limitations, there is a demand for techniques that can measure rapid recrystallization kinetics in a non-destructive, real-time manner. Here, in situ synchrotron XRD is a promising technique where the development of ultra-fast detectors has enabled XRD to achieve high temporal resolution, making it particularly well-suited for studying rapid processes, such as laser-based processing methods [13]. Synchrotron XRD offers versatile capabilities as it can be used to monitor lattice strain evolutions, texture variations, and other important diffraction-peak features that are associated with aspects of recrystallization. Previous work by Navarre et al. correlated various aspects of the physical phenomena involved in recrystallization with XRD data obtained during operando synchrotron measurements [14]. Still, the application of synchrotron XRD to study such phenomena is constrained by the limited accessibility of the technique. This means that while it can capture the dynamic nature of recrystallization, it is more suited to help establish a ground-truth of the phenomena rather than be used for larger scale analysis or adaptation.

Various alternative approaches have been explored for real-time characterization and monitoring of material processing at elevated temperatures. These include pyrometers, laser-ultrasonics, thermal cameras, photodiodes, and acoustic emission (AE) sensors [15,16]. Among these techniques, AE sensors have gained favour due to their low cost, non-destructive nature, high temporal resolution, and high sensitivity when detecting internal structure variations [17]. This technique is based on acquiring acoustic signals via airborne or structure-borne sensors that are positioned around the process zone and correlating the emitted acoustic signatures to specific process regimes [18,19]. The efficiency of this technique depends on signal characteristics such as frequency and intensity threshold, the metallurgical state of the sample (e.g., crystalline structure, composition, and grain morphology), and the experimental setup used during measurements. In particular, the evolution of microscopic defects is expected to be within the frequency range of 100 kHz to 1 MHz [17]. Scruby et al. [20] as well as Schaarwächter and Ebener [21] demonstrated that AE can detect high-velocity dislocation motion and fracture dissipation in the context of plastic deformation and microcracking. While Frederick and Felbeck [22] showed that the unpinning of dislocations and the activation of dislocation sources could result in observable AE. Their work further showed that the most significant emission occurs during stress application, with abrupt stress relaxation being detectable using sensitive piezoelectric transducers. Further studies by Chen et al. [23,24] have advanced the use of AE spectroscopy, which acquires burst AE signals rather than continuous signals. These works showed that during tensile testing [23,25], AE spectroscopy could detect and isolate acoustic activity of dislocation movement, entanglements, and twinning processes. AE monitoring has also been successfully applied in laser processing of composites, including the evaluation of heat-affected zones in CFRP cutting [26] and the guidance of high-quality blind-hole drilling in CFRP/Cu laminates through advanced frequency-domain analysis [27]. These studies demonstrate that AE can be extended beyond defect detection toward detailed monitoring of thermal and mechanical interactions during processing. A recent study by Esmaeilzadeh et. al [28] even indicated that AE spectroscopy could be used to detect distinct AE signature of the martensitic transformation during additive manufacturing of Ti6Al4V-Fe alloys. However, despite the mentioned developments, the use of AE techniques to study and detect the stages of recrystallization has yet to be presented in literature.

The utilization of AE to follow physical phenomena such as recrystallization represents an important advancement, as it would enable real-time monitoring without reliance on large-scale facilities. However, to establish reliable correlations between AE signatures and recrystallization a ground truth is required. Synchrotron XRD offers an excellent option in this regard, as its fast acquisition rates allow real-time tracking of recrystallization dynamics [14]. The recent development of a laser-based processing device for synchrotron experiments makes it possible to synchronize AE and XRD measurements during laser processing [13,29]. This device has already been used with AE sensors to classify defects [15], detect porosity healing [30], and monitor melt pool stability [31], demonstrating its capability for combined operando studies. By enabling simultaneous acquisition of AE and XRD signals, the device provides a platform to directly investigate how recrystallization dynamics can be related to changes AE signal activity.

Building on this, the present work addresses the gap in the literature by exploring, for the first time, the correlation between AE signals and the stages of recrystallization during laser-induced heat treatment. Using cold-rolled 316L stainless steel as a model material, AE activity was monitored concurrently with in situ synchrotron XRD measurements during laser scanning. This approach allows AE data to be interpreted against a well-established XRD framework for recrystallization [14], thereby assessing the potential of AE as a method for real-time monitoring of recrystallization phenomena.

2. Methods

2.1. Material

For the recrystallization specimens, an AISI 316L stainless steel plate with an initial thickness of 15 mm was subjected to multi-pass cold rolling, achieving a final thickness reduction of 80 %. The rolled plate was further sectioned into 20 mm × 30 mm × 1.1 mm samples. The composition of the material was measured using an Ultra 55 SEM (Zeiss, Germany) equipped with an energy dispersive spectroscopy (EDS) detector (Oxford, United Kingdom), see Table 1.

2.2. Laser processing

Laser-induced heat treatments (LHT) were conducted using the miniSLM which is a miniaturized laser powder bed fusion (L-PBF) machine [13,29]. The LHT experiments were conducted in a chamber continuously flushed with argon gas (99.998 %), maintaining an oxygen level below 200 ppm within the processing chamber. The optimization of LHT parameters was based on [14], using the concept of normalized enthalpy [32]. The laser beam was negatively defocused to a spot radius of 182 μm (at $1/e^2$) to maximize heat input and to optimize the spatial distribution. Using a unidirectional parallel scanning strategy, multiple laser passes were applied to a rectangular area of 1.1 mm × 2.915 mm to extend the heat treatment duration. LHT was performed at normalized enthalpy values below 1 to avoid surface melting. Table 2 provides a comprehensive overview of the absorptivity values, laser parameters and normalized enthalpy values used for this investigation. The laser absorptivity of the 316L stainless steel samples was measured using an UV/VIS/NIR Spectrometer Lambda 950 (Perkin Elmer, USA).

Table 1
Chemical composition of the cold-rolled 316L stainless steel samples as measured by EDS.

	Fe	Cr	Ni	Mo	Mn	Si
316L SS	Bal.	18.1 ± 0.3	12.6 ± 0.5	2.8 ± 0.4	1.0 ± 0.3	1.0 ± 0.2

Table 2
Utilized parameters and material properties for the laser-induced heat treatments of the 316L specimens.

Laser Spot Radius (μm)	Laser Power (W)	Scan Speed (mm/s)	Hatch Distance (μm)	Number of scans	Absorptivity	Normalized Enthalpy (J)	Duration (s)
182	45	1000	60	415	0.41	0.31	29.1

2.3. Operando X-ray diffraction

Operando X-ray diffraction experiments were conducted at the P23 beamline at the PETRA III DESY synchrotron radiation source. The miniaturized L-PBF device was mounted on a dedicated stage and inclined at 17° relative to the incident X-ray beam. A focused X-ray beam with an energy of 20.5 keV was employed. The resulting projected spot size on the sample was 300 × 342 μm^2. The data were acquired using an Eiger 500 k detector (PSI, Switzerland) at a frequency of 500 Hz with an exposure time of 0.002 s, with the detector beginning acquisition approximately 100 ms before the onset of laser scanning. A schematic of the device configuration within the X-ray beam and area where the X-ray beam, laser beam, and stainless steel sample interact are presented in Fig. 1. The z-axis was aligned with the laser axis, while the x-axis was parallel to the laser scanning direction, and the y-axis was perpendicular to the laser scanning direction.

2.4. X-ray diffraction data analysis

Initially, the captured 2D X-ray diffraction data were azimuthally integrated using pyFAI [33] to reduce the data into 1D diffraction patterns. Next, monitoring the recrystallization kinetics was done by narrowing of the (200) successive XRD peaks that were collected from the experiments. The full width at half maximum (FWHM) of each peak was evaluated by fitting the diffraction peaks using a split Pearson VII function. For such qualitative analysis, the instrumental broadening was not deconvoluted from the data, as only the relative change in the diffraction peaks was examined and not the absolute change. Additional filtering was applied to remove spikes in the FWHM observed in the experimental data, see Fig. S1 in the Supplementary Material. These spikes occur when the laser is near the X-ray measurement area, leading to large temperature gradients and a corresponding increase in FWHM. Since our analysis focused on changes in slope rather than absolute values, these spikes were excluded as they were not relevant to these calculations.

Previous work by Navarre et al. [14] established that taking the evolution of the FWHM of X-ray diffraction peaks (particularly the change in slope) serves as an effective indicator for monitoring the four distinct stages of recrystallization, see Fig. 2. Upon initiation of the LHT (stage 0), there is a rapid increase in temperature resulting in a sharp drop in FWHM. This abrupt change is attributed to the immediate thermal response of the crystal structure to the intense laser energy input. In Stage I, dislocations start reorganizing and annihilating. This phase is characterized by a gradual peak narrowing, primarily due to the decrease in dislocation density. The decrease in FWHM during Stage I is less pronounced than in Stage 0 but lasts over a longer period. The onset of nucleation marks the transition to Stage II. This stage is distinguished by a pronounced narrowing of the diffraction peaks, which can be attributed to two main factors. First, to an increase in the size of coherent scattering regions, as the newly formed nuclei expand. Second, to a more rapid decrease in dislocation density, consumed by the advancing boundaries of the growing crystals [34]. This stage is in fact the recrystallization process itself. Then during the final Stage III, fine recrystallized grains have replaced the strain-hardened regions near the surface of the sample. These grains continue to grow at a reduced rate. The FWHM continues to decrease, but with a less steep slope compared to Stage II. Again, this moderation in rate of change can be attributed to two competing processes. First, to the formation of annealing twins, which introduces new crystallographic orientations and potentially new grain boundaries [5]. Second, to the slower progression of recrystallization in deeper regions of the sample, where thermal energy dissipation results in lower temperatures. The end of the recrystallization process is defined as the point when no further change in the FWHM is observed and the slope of the FWHM curve reached zero.

To determine the temperature history during the LHT, the integrated 1D data was fitted using in-house developed MATLAB scripts. These scripts were used to extract peak positions prior to the LHT and to track their changes during the LHT. From the in situ XRD data, the lattice strain evolution was determined by measuring the relative change in the peak position (2θ). This is done by determining the lattice strain (ε) following Bragg's law (1):

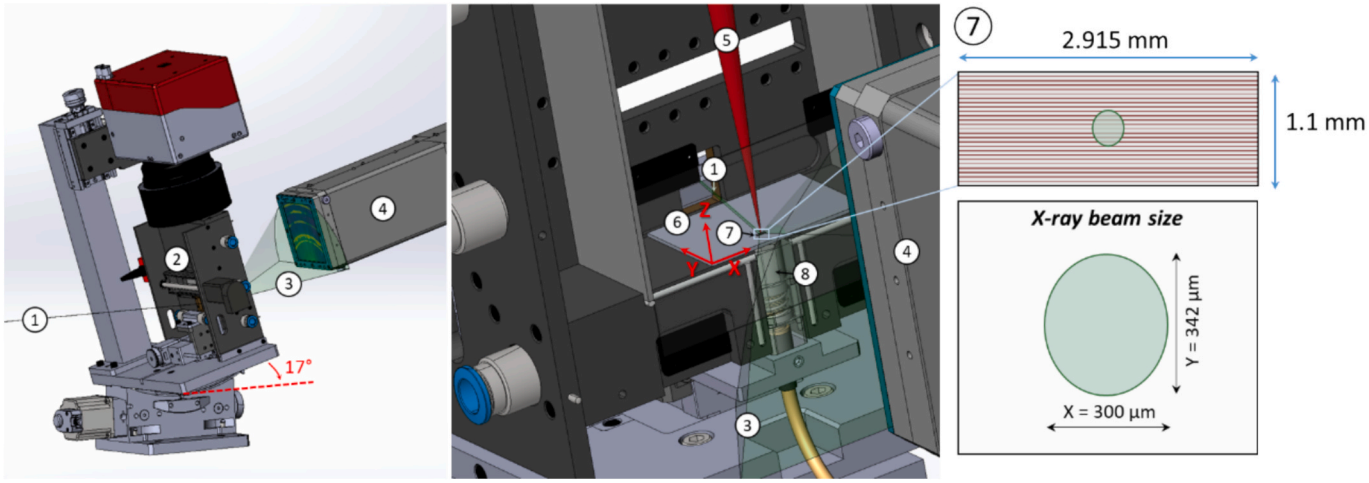

Fig. 1. Schematic of the experimental setup used during operando X-ray diffraction measurements. Within this figure the following numbers indicate; 1. Incident X-ray beam; 2. Miniaturized L-PBF device; 3. Diffracted X-ray beam; 4. X-ray detector; 5. Laser beam; 6. 316L SS rolled sample; 7. Laser heat treated zone; 8. Structure-borne acoustic emission sensor.

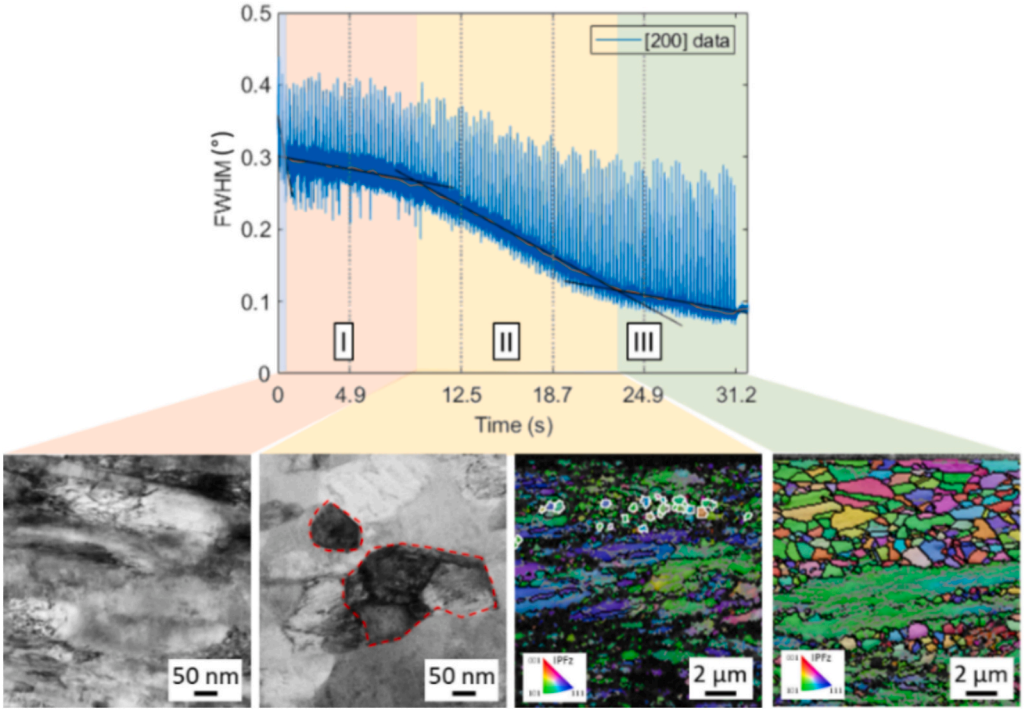

Fig. 2. Evolution of the FWHM of the (200) diffraction peak as a function of time during the LHT. The corresponding microstructures at each stage of recrystallization as taken from [14]. Stage I is indicated by the orange region, Stage II is indicated by the yellow region, and Stage III is indicated by the green region.

$$\varepsilon = \frac{\sin(\theta_0)}{\sin(\theta)} - 1 \tag{1}$$

where θ is half of the diffraction angle, θ_0 is half of the diffraction angle that corresponds to the reference state and was defined by the peak position at the beginning of each measurement prior to laser scanning. Assuming that changes in the lattice strain were primarily due to thermal effects, it was then possible to calculate the average temperature within the illuminated volume of the X-ray beam. As the temperature could be correlated to strain by the temperature-dependent thermal expansion coefficient (2):

$$T(t) = \alpha_L(\varepsilon) \tag{2}$$

Where T(t) is the temperature within the probed region and $\alpha_L(\varepsilon)$ is a strain-dependent thermal expansion coefficient function to convert strain into temperature. The thermal expansion behaviour of 316L was determined based on previous measurements by Desai et al. [35]. The corresponding strain-dependent thermal expansion coefficient function for 316L SS is provided in Supplementary Material see Fig. S2. XRD peak shifts are influenced not only by temperature but also by factors such as mechanical strain [36] and composition [37]. Although these effects cannot be entirely excluded, earlier work has demonstrated good agreement between thermal histories derived from in situ XRD and those predicted by simulation [38], supporting the conclusion that temperature is the dominant factor. While the specific temperature values extracted from XRD peak shifts should not be regarded as exact, they provide an indication of the correct magnitude of heating rate and maximum temperature. This makes them a useful basis when comparing differences in recrystallization kinetics between specimens.

When plotting the temperature history during the LHT, a Savitzky-Golay filter with a window size of 20 and a polynomial order of two was utilized to smooth the data. The temperature history during LHT for each sample without the filter is provided in the Supplementary Material Fig. S3.

2.5. Acoustic emission data acquisition

In this work, in situ acoustic emission sensing was utilized to study the acoustic signature of recrystallization based on a structure-borne sensor. The VS370-A3 passive piezoelectric AE-sensor (Vallen System, Germany), featuring a compact design with a threaded housing, was used. This sensor exhibits sensitivity within the frequency range of 150 to 600 kHz. The sensor was positioned directly beneath the process zone to optimize capturing acoustic events within the material. A customized design incorporating a spring mechanism was implemented to push the sensor upwards and ensure coupling with the sample, as illustrated in Fig. 1 (see label 8). A polymer coupling paste was applied at the sensor-sample interface for better signal-to-noise ratio. The signals from the laser scan head controller and the acoustic sensor were acquired separately using two channels of an Advantech PCIE-1840 Data Acquisition card within a dynamic range of ± 10 V, at a sampling rate of 1.53 MHz. This sampling frequency was selected to satisfy the Nyquist Shannon theorem, which indicates that the frequency must be at least two times the sensitivity range of the sensor [39]. Channel 0 was assigned to the laser scan head controller, giving the laser signal modulation according to the scanning status (0 V = laser off; 5 V = laser on). Channel 1 was assigned to record the AE signals from the structure-borne sensor. The acoustic signal acquisition was automatically triggered based on the laser signal; as soon as the laser signal exceeds 0.5 V, the data acquisition starts for all channels, resulting in their synchronization; the files are stored separately for further offline analysis. The AE data were segmented into windows of 4000 data points, corresponding approximately to the duration of a single scan track at a scan speed of 1000 mm/s and a sampling rate of 1.53 MHz. This segmentation ensures that each window represents the steady-state portion of the process, avoiding transient effects during the initial acceleration and final deceleration phases. The segmented data were then filtered and processed using fast Fourier transform (FFT) functions to extract features in the time–frequency domain. To enhance spatial correspondence with the synchrotron XRD measurements, analysis specifically focused on the laser scan track that directly overlapped with the area probed by the X-ray

beam. Although multiple adjacent tracks were scanned, this approach ensured that the AE data primarily represented acoustic activity originating from the same localized region probed by XRD.

2.6. Post-Mortem microstructure characterization

To evaluate if recrystallization occurred within each of the samples after LHT, electron backscatter diffraction (EBSD) was conducted using a ZEISS Gemini SEM II microscope (Carl Zeiss AG, Germany). Prior to EBSD, the samples were prepared as vertical cross-sections, perpendicular to the laser scanning direction. These cross-sections were subsequently ground using SiC abrasive papers up to 2500 grit size, followed by polishing with silica particle suspension to a fineness of 0.25 µm. During EBSD measurements, an accelerating voltage of 25 kV and a step size of 95 nm were used. From the collected EBSD data, kernel average misorientation (KAM) maps were extracted using the Aztec acquisition software (Oxford Instruments, UK). These maps were used to determine if recrystallization had occurred within each of the samples by considering that KAM values between 0 and 0.5 indicated that recrystallization had occurred within the samples.

3. Results and discussion

3.1. Stages of recrystallization during laser heat treatment

The recrystallization kinetics were initially assessed by examining the evolution of the FWHM during LHT, as shown in Fig. 3. To determine the times marking the onset of nucleation (t1), the initiation of grain growth (t2), and the completion of recrystallization (t3) fitted tangents were overlaid onto the plotted data based on changes in slope. The intersection points of these tangents were used to define each transition time. For the three stages of recrystallization, each tangent was drawn according to specific slope variations. The tangent marking the end of recrystallization originates from the point where the FWHM curve first reached zero. For Samples 1, 2 and 5, the start of nucleation (1.8 s, 2.2 s, and 1.4 s), grain growth (7.9 s, 8.9 s, and 7.2 s), and end of recrystallization (17.7 s, 18.9 s, and 17.9 s) occurred at relatively similar times during the LHT. In contrast, Sample 3 exhibited delayed recrystallization stages during the LHT, with nucleation (3.5 s), grain growth (12.3 s), and recrystallization (23.4 s) completely after a longer time. While Samples 4 and 6 showed significantly faster kinetics during the LHT, with nucleation (0.5 s and 1.0 s), grain growth (2.8 s and 3.9 s), and recrystallization (11.7 s and 12.3 s) completing after a shorter time.

To understand the differences in the observed recrystallization kinetics between the various samples, the temperature history during LHT was extracted from the collected XRD data, see Fig. 4. This analysis revealed clear correlations between thermal history and recrystallization behaviour. For samples 1 and 2, the initial heating rate and average temperature were similar, explaining their comparable recrystallization kinetics. In contrast, sample 3 had the slowest initial heating rate and lowest average temperature, resulting in the slowest recrystallization kinetics and the longest recrystallization time. Conversely, sample 4 and 6 demonstrated the fastest initial heating rate and the highest average temperature during LHT, explaining their rapid recrystallization kinetics and the shortest recrystallization time. Sample 5 was a bit of an outlier, exhibiting a slower heating rate and a maximum peak temperature similar to what was observed for sample 3. While this deviation is notable, such variability can occur under experimental conditions and remains within an acceptable range for the purposes of this study. The presented thermal history also shows that while all samples were processed using the same parameters, there were noticeable differences in the measured thermal history as well as recrystallization kinetics. These

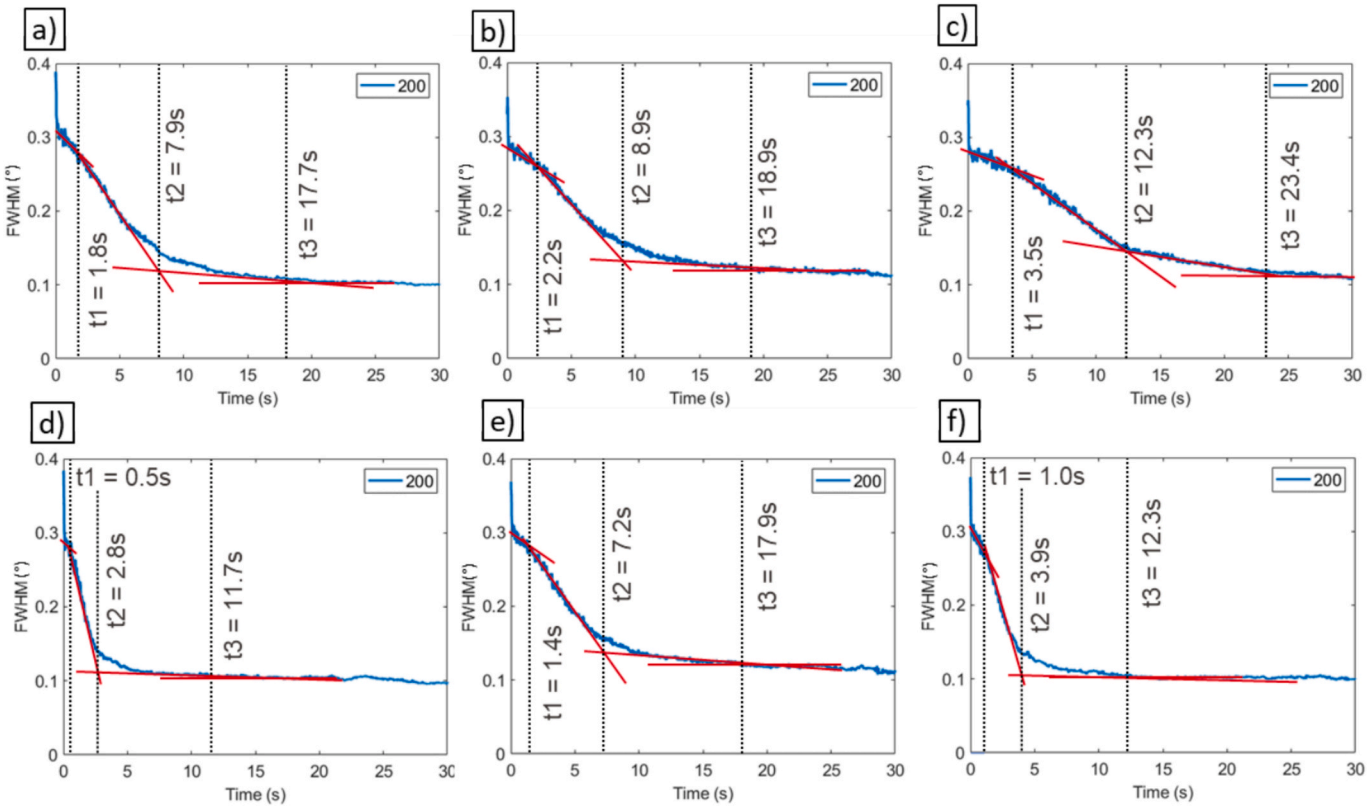

Fig. 3. Evolution of the full width half maximum (FWHM) over time for the (200) peak for: a) Sample 1, b) Sample 2, c) Sample 3, d) Sample 4, e) Sample 5, and f) Sample 6. The fitted tangents of the three stages of recrystallization are plotted in red. The intersection of these tangents, corresponding to the change in slope of the curve, are indicated with black dotted lines, and indicate characteristic recrystallization times; *t*1: start of nucleation, *t*2: start of grain growth, and *t*3: end of recrystallization.

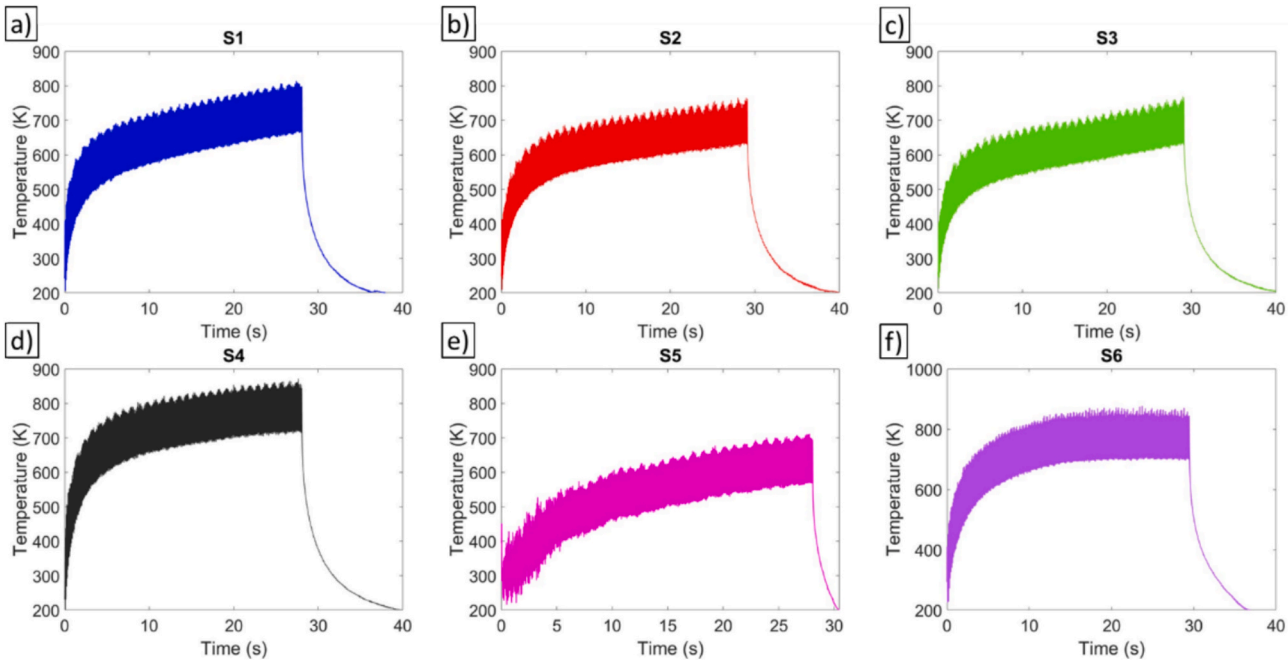

Fig. 4. Temperature history during LHT from in situ XRD measurements after Savitzky-Golay filtering for: a) Sample 1, b) Sample 2, c) Sample 3, d) Sample 4, e) Sample 5, and f) Sample 6.

variations in part can be attributed to non-uniform surface roughness across the sample set [40], which influences laser energy absorption and leads to localized variations in heat input during LHT [41]. Additionally, slight deviations in sample dimensions (even on the micron scale) can alter the laser spot size and modify energy the intensity, thus affecting thermal history.

After the LHT, KAM maps were obtained via EBSD to assess the occurrence of recrystallization, see Fig. 5. Before LHT, the cold-rolled 316L stainless steel samples exhibited KAM values ranging between 1.5 and 3, indicating significant local plastic strain and a high geometrically necessary dislocation density. In contrast, post-LHT, the samples displayed noticeably lower KAM values, within the range of 0 to 0.5. This change in KAM values reflect minimal misorientation within the grains after LHT and confirm that significant recrystallization had taken place within the 316L specimens during the LHT.

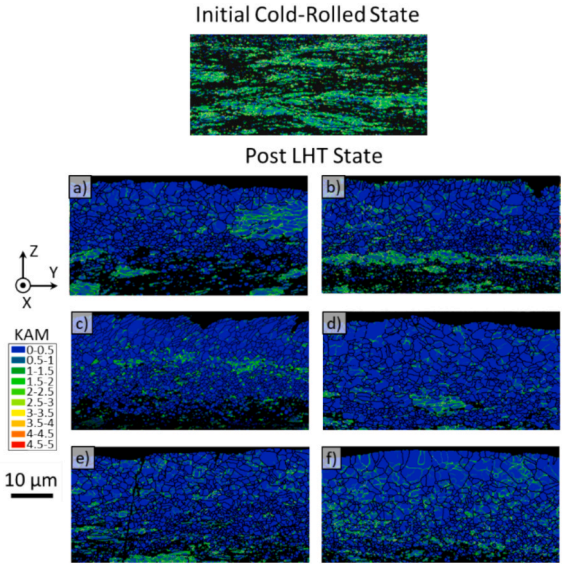

Fig. 5. EBSD analysis showing kernel average misorientation (KAM) maps for an initial cold-rolled sample and for the post-LHT state for: a) Sample 1, b) Sample 2, c) Sample 3, d) Sample 4, e) Sample 5, and f) Sample 6.

3.2. *Acoustic emission signal analysis*

Fig. 6 shows the temporal evolution of raw acoustic signals obtained from the laser trigger and the acoustic sensor. The green inset provides a magnified view of the laser trigger signal, revealing square waves that correspond to individual laser line scans. The precise synchronization between AE data and the laser trigger allows for an accurate temporal correlation of AE events to the laser processing stages. Analysis of the AE signal amplitude reveals that the most intense acoustic activity occurs within the initial 10 s of the process. This observation aligns with the gradual progression of microstructural changes typically associated with recrystallization phenomena. However, the presence of a significant background noise, denoted by yellow dashed lines, underscores the necessity for more sophisticated data analysis techniques. Specifically, exploration of the time–frequency domain may yield more valuable information.

When representing the acoustic signals in the frequency domain, it was possible to reveal its periodic components [42]. The power spectrum density (PSD) distribution was calculated for all frequencies using FFT signal decomposition and implementing the Welch method [43] using windows of 2.7 ms. Time localization of frequencies was achieved by combining the FFT plots of each time window, see Fig. 7. This spectral analysis revealed three prominent frequency ranges across all samples, centered approximately around 94, 188, and 282 kHz, see Fig. 7a. These frequencies appear as near-integer multiples of one another, suggesting harmonic relationships within the detected acoustic response. Accordingly, the 94 kHz and 282 kHz peaks are interpreted as secondary responses associated with the dominant 188 kHz component, rather than independent resonances. While the dataset was limited to six samples, the dominant ~ 188 kHz AE component was consistently observed in all specimens, demonstrating repeatability within the available experimental scope.

The 94 kHz peak was not analyzed further, as it lies below the lower bound of the sensor's optimal sensitivity range (< 100 kHz). Among the remaining components, the 188 kHz frequency consistently exhibited

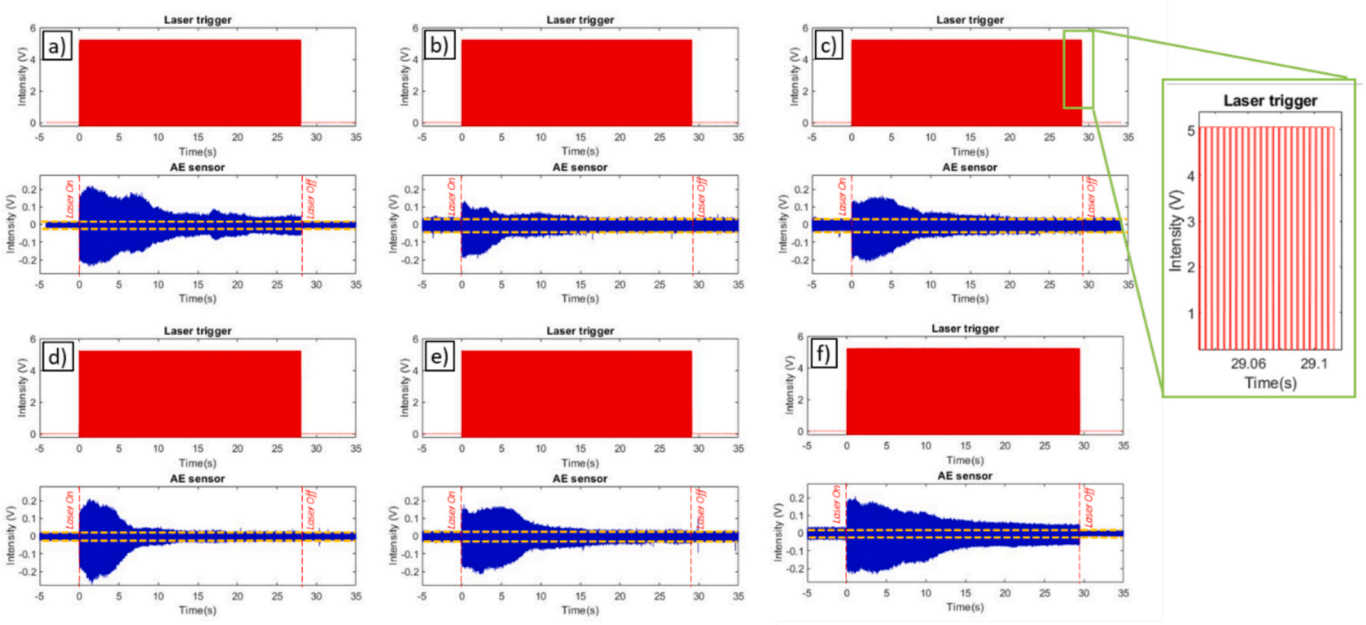

Fig. 6. Temporal evolution of the raw signals from the two synchronized channels: laser trigger (shown in red) and AE sensor (shown in blue) for: a) Sample 1, b) Sample 2, c) Sample 3, d) Sample 4, e) Sample 5, and f) Sample 6. Background level is delimited using yellow dashed lines.

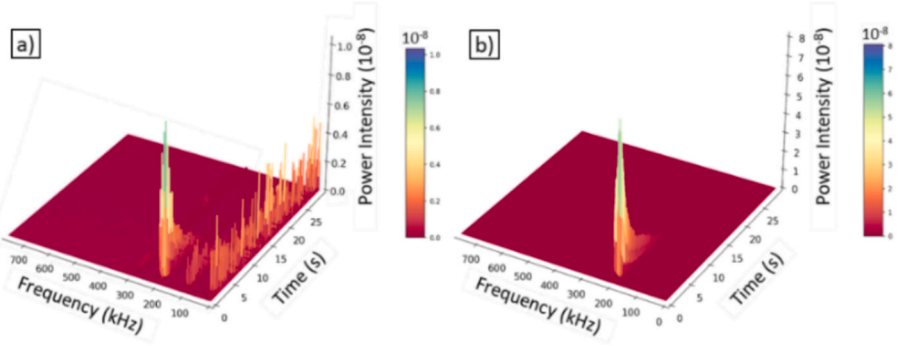

Fig. 7. Filtered AE data from sample 1: a) before empirical mode decomposition (EMD), and b) after empirical EMD.

the highest amplitude and superior signal quality across all measurements, making it the most robust and reproducible feature for subsequent AE analysis. Empirical mode decomposition (EMD) was subsequently applied to the raw signal to isolate the most relevant frequency components (~188 kHz) and mitigate background noise. This technique decomposes the signal into intrinsic mode functions (IMFs) [44], of which only the first IMF, representing the signal's highest frequency component, is retained. The result of this filtering is shown in Fig. 7b, while Fig. 8 presents the plots of the filtered data for all examined samples.

The identified frequencies should not be interpreted as structural resonances of the specimen. As if they had originated from vibrational modes, small variations in the sample geometry, placement or other boundary conditions would have produced measurable frequency shifts between samples. Instead, the AE spectra remained consistent across all experiments. This indicates that the 188 kHz component represents the dominant frequency peak of the examined cold-rolled 316L stainless steel under the present experimental conditions. Although the specific cause of this frequency's sensitivity to recrystallization remains unclear, its consistent correspondence with the XRD identified stages of recrystallization demonstrates that it was the most reliable frequency range that could be correlated to the ground-truth data.

It is important to consider whether the observed AE activity at ~ 188 kHz might originate from factors other than recrystallization such as laser-induced vibrations, instrumental noise, or thermally induced stress relaxation. The persistence of AE activity throughout the entire laser exposure period (~30 s) suggests a limited contribution from laser-induced vibrations, as a more constant response would be expected if vibrations were dominant, see Fig. 8. Instrumental artifacts are also unlikely, as functionality checks of the AE sensor were performed prior to each experiment to ensure stable and reliable acquisition in the absence of laser exposure. Thermally induced stress relaxations, however, are inherently linked to recrystallization, as they arise from the release of stored strain energy during dislocation motion, rearrangement, and annihilation. Therefore, while the dominant AE response in this frequency range is attributed to recrystallization, some coupled thermal relaxation effects are also likely present within the captured signal.

3.3. Correlation of acoustic emission & X-ray diffraction data

To facilitate the correlation between AE and XRD data, the PSD at a frequency of 188 kHz was plotted over time for each sample, see Fig. 9. Characteristic times relating to the onset of nucleation and grain growth as well as the end of recrystallization (taken from Fig. 3) have been added to this figure to reveal important dynamics associated with each

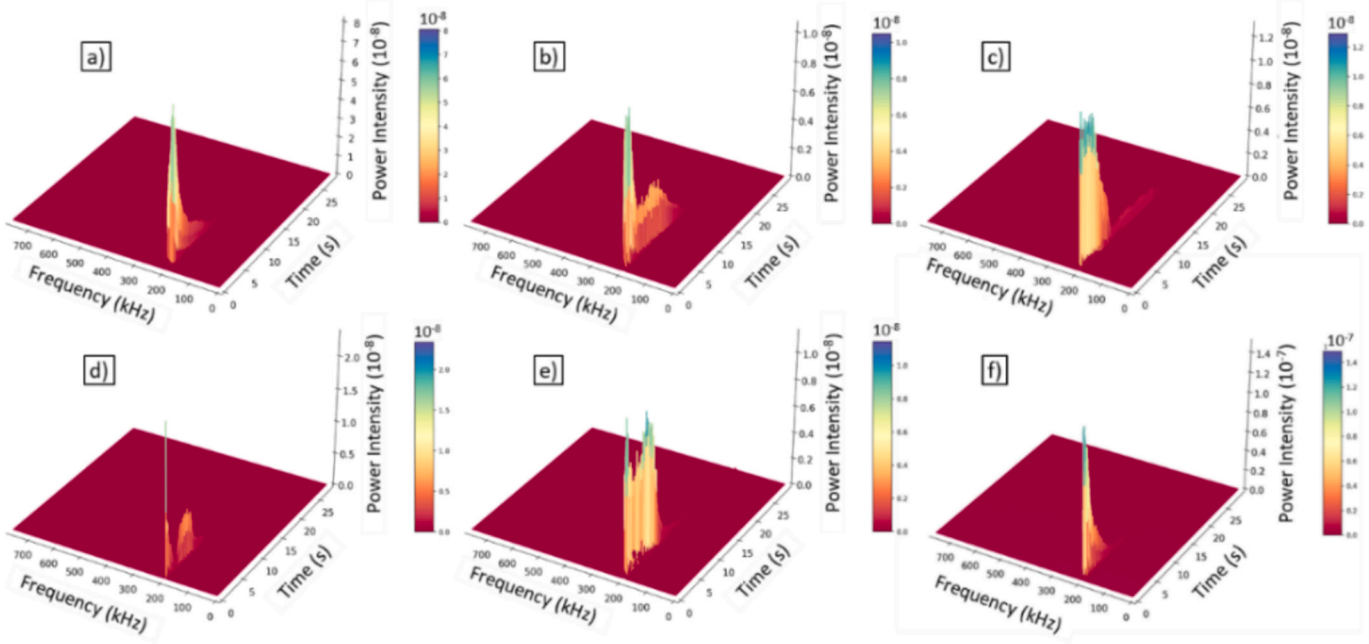

Fig. 8. Filtered AE data plots for all examined samples after empirical mode decomposition (EMD) for: a) Sample 1, b) Sample 2, c) Sample 3, d) Sample 4, e) Sample 5, and f) Sample 6.

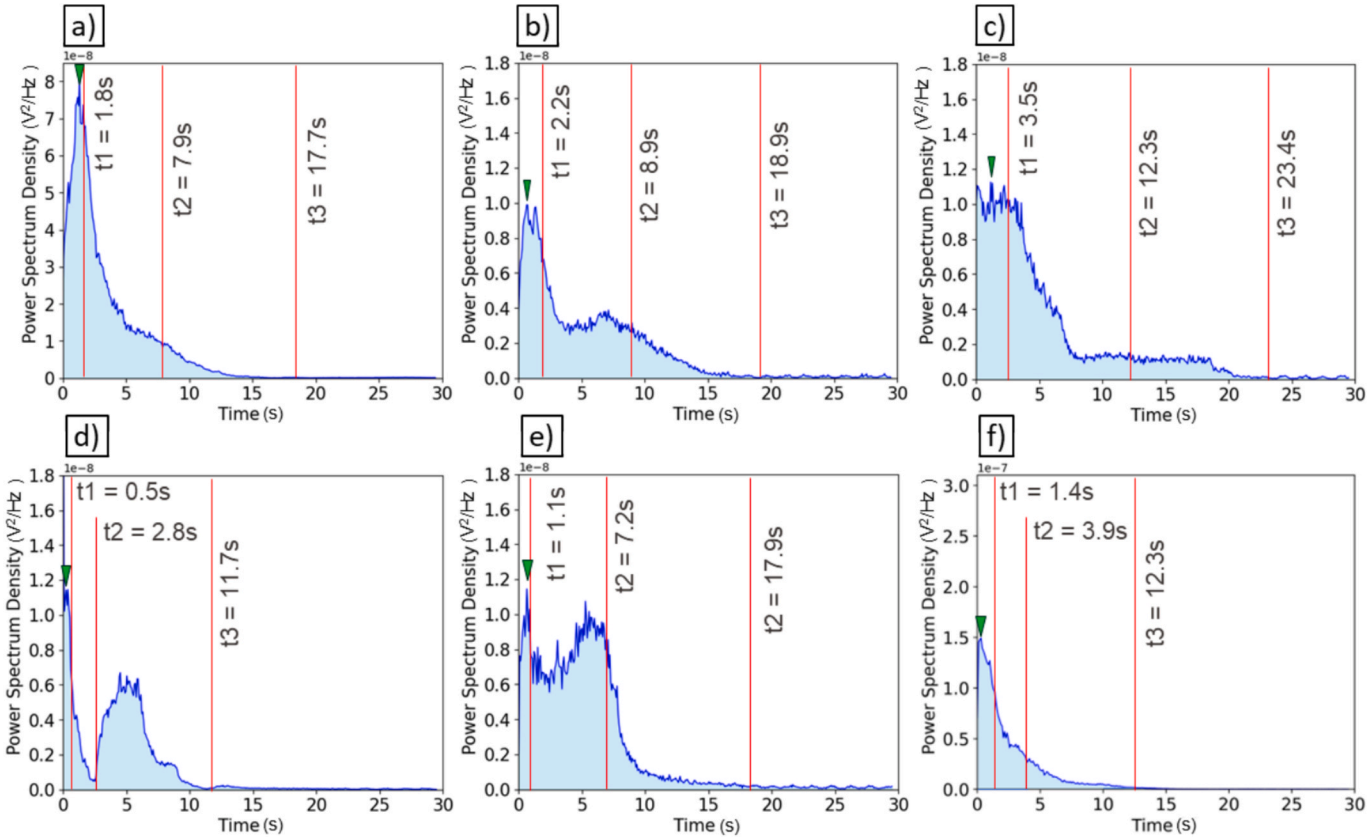

Fig. 9. Power spectrum density (PSD) of the acoustic emission (AE) data at a frequency of 188 kHz as a function of time for: a) Sample 1, b) Sample 2, c) Sample 3, d) Sample 4, e) Sample 5, and f) Sample 6. The green arrow represents the maximum intensity peak within the AE data, while the red lines are used to outline the characteristic recrystallization times *t*1, *t*2, and *t*3 determined in Fig. 4 which indicate the: *t*1: start of nucleation, *t*2: start of grain growth, and *t*3: end of recrystallization.

stage of recrystallization.

The work of Frederick and Felbeck [22] emphasized the necessity of reaching a stress level threshold to activate acoustic wave release, which underlines the significance of Stage 0 in achieving appropriate stress level for the acoustic signals to be detected. Their work also established a direct proportionality between acoustic activity and grain boundary density. In the following discussion, the PSD intensities from the current experiments, in relation with the XRD data, were interpreted based on their findings.

At the beginning of LHT, there is an abrupt increase in the AE signal. This is likely due to the high initial dislocation density of the samples, see Fig. 5, coupled with the rapid nature of heating during the LHT, which can induce local plastic deformation. Combined, these factors will cause dislocations to move, entangle and annihilate, generating noticeable AE signals within the material [24,25]. As the temperature increases, preliminary recovery processes operate during Stage I, before the onset of recrystallization. Near the end of Stage I, AE peaks with high intensity begin to appear. Their formation is likely due to the complex phenomena involved in the formation of dislocation-free crystallites. These phenomena, which collectively change the stress field and stored energy just prior to nuclei formation, include: enhanced dislocation climb and reorganization freedom, improved annihilation at cell walls, high-angle grain boundary bulging, formation and migration of sub-grain boundaries around quasi strain-free regions, and changes in misorientation of these sub-grain boundaries [2,34]. The cumulative effect of said phenomena can result in the generation of stronger acoustic pulses. The onset of nucleation (Stage II) occurs shortly after the maximum AE intensity peak. As the process transitions into Stage II, the PSD begins to decline, continuing to decrease beyond this stage and until reaching Stage III (grain growth). This decline is associated with nuclei formation and subsequent growth, involving the formation and motion of high-angle grain boundaries, leading to a gradual decrease in grain boundary density. The consumption of dislocations by the moving boundaries still produces AE signals, however their global number decreases, and the internal stress field progressively vanishes. Eventually, when the consumption of dislocations by moving boundaries ends and the recrystallization process finishes, acoustic emission signals are no longer captured. When using such distinctions to identify the end of recrystallization, variability between samples must be considered. Stabilization of the AE signal provides an indication of completion, but allowing a short additional period (~5 s) beyond this point offers greater confidence that recrystallization has finished when using such measurements for real-time monitoring. A continuous decline in PSD after reaching a high-intensity peak was not observed in all samples. As for sample 2, the PSD plateaued and slightly increased before resuming its downward trend. Similarly, for samples 4 and 5, an intermediate increase in PSD was followed by a brief plateau and a subsequent decrease before recrystallization was completed.

From these correlations of XRD and AE data, the most encouraging finding is that specific AE signals can be used to determine the onset of recrystallization and when additional laser processing does not induce further recrystallization. This provides a method to ensure desired microstructural changes (e.g., improved ductility, corrosion resistance, stress relief, and refined grain structure) are achieved without risking unnecessary grain growth. Furthermore, AE can optimize LHT processes by minimizing energy consumption while maintaining mechanical and corrosion performance. Notably, the results of this study show that the required recrystallization time varies even with the same material and processing conditions. By using AE to precisely identify the completion of recrystallization, components can be repaired and refurbished more efficiently in laser-based processes.

While promising, the current experimental approach also involves some important considerations, particularly the mismatch in the spatial sensitivity of the employed techniques. The AE sensor captures activity from the entire sample, whereas the synchrotron XRD measurements probe only a small, localized volume. To minimize this spatial mismatch, the AE signal analysis concentrated on the laser scan track that directly overlapped with the XRD measurement region. Focusing on the overlapping track allowed the AE data to more closely represent activity from the same localized area. Nonetheless, AE remains a bulk technique, and a certain degree of spatial averaging is unavoidable. Therefore, correlations between the two methods should be interpreted within this context. This can also potentially explain why certain transitions were less distinctly captured by AE compared to XRD. While AE signals clearly marked the onset of Stage II (nucleation and growth of new grains), transitions into Stage I (dislocation rearrangement) and Stage III (grain growth) were not as well resolved. Both stages occur in a spatially heterogeneous and temporally staggered manner, as local variations in thermal history cause different regions of the material to undergo dislocation rearrangement or grain growth at different times. Consequently, signals originating from different regions become partially superimposed, leading to a convoluted AE response. Unlike the clear stage transitions that were observed by XRD.

The presented findings represent the first reported attempt to correlate acoustic signatures with recrystallization using operando XRD data. The observed correlation between AE and XRD demonstrates that AE signals can serve as a non-destructive method for real-time monitoring of recrystallization stages, particularly for determining the time required for recrystallization to occur. Notably, this method can operate at depths beyond the reach of X-ray analysis, making it a versatile tool for studying this type of material behaviour. Such findings pave the way for further development of efficient real-time monitoring techniques that can advance our understanding of the recrystallization process.

In this work, synchrotron XRD was used as a ground truth to validate the correlation between AE signals and recrystallization dynamics. While such in situ synchrotron measurements are not practical in industrial environments, the established framework provides a basis for transferring this methodology to laboratory and production-scale systems. Future studies can extend this approach to other alloys and geometries to further refine AE and recrystallization relationships under relevant processing conditions, thereby supporting the development of AE as a real-time monitoring tool for recrystallization.

Looking ahead, further studies are required to resolve recrystallization stages in greater detail and to extend this approach to other alloys and geometries. In more complex materials, recrystallization may involve additional mechanisms and produce different AE responses, which must be systematically investigated before a broader generalization of this approach can be achieved.

4. Conclusion

This study introduces a novel approach for online monitoring of laser-induced recrystallization in cold-rolled 316L steel using AE signals. Our findings demonstrate the potential of AE as a non-destructive, real-time monitoring tool for tracking the dynamics of the recrystallization process. Key outcomes include:

1. Development of a framework for interpreting XRD data and correlating it with the thermal history during laser-induced recrystallization.
2. Identification of a dominant frequency that can be associated with microstructural changes during recrystallization. This dominant frequency can be identified by filtering the raw AE data using a combination of power spectrum density distribution analysis via fast Fourier transforms, harmonic identification, and empirical mode decomposition. For the current experimental set-up and sample geometry, this dominant frequency was measured at ~ 188 kHz. For other sample geometries and materials, the expected range of the dominant frequency can be estimated by calculating the theoretical fundamental frequency based on material properties and boundary conditions.

3. Correlation of AE signals with ground-truth XRD data, enabling the detection of key events during recrystallization, such as the onset of nucleation as well as the completion of the recrystallization process.

These findings establish AE as non-destructive method that can achieve real-time monitoring of events during recrystallization. This paves the way for more precise and efficient laser processing, offering enhanced microstructural control during laser processing and reducing the risk of excessive grain growth during heat treatment. Looking ahead, further studies across different alloys and geometries will help expand the applicability of this approach and uncover new opportunities for AE-based monitoring of complex recrystallization behaviour.

CRediT authorship contribution statement

Claire Navarre: Writing – original draft, Methodology, Investigation, Formal analysis, Conceptualization. **William Hearn:** Writing – review & editing, Writing – original draft, Methodology, Investigation, Formal analysis. **Mathijs Van der Meer:** Writing – review & editing, Visualization, Methodology. **Lucas Schlenger:** Writing – review & editing, Investigation. **Rik Vaerenberg:** Formal analysis. **Nicolas Mari:** Writing – review & editing, Formal analysis. **Reza Esmaeilzadeh:** Investigation. **Amir M. Jamili:** Investigation. **Vigneashwara Pandiyan:** Writing – review & editing, Formal analysis. **Steven Van Petegem:** Writing – review & editing, Supervision, Investigation, Funding acquisition, Formal analysis, Conceptualization. **Roland E. Logé:** Writing – review & editing, Supervision, Methodology, Funding acquisition, Conceptualization.

Funding

This work was supported by the Swiss National Science Foundation (SNSF) [grant number 20211121_193799].

Declaration of competing interest

The authors declare that they have no known competing financial interests or personal relationships that could have appeared to influence the work reported in this paper.

Acknowledgements

The authors would like to acknowledge the financial support of PX Group to the EPFL LMTM laboratory. We acknowledge DESY (Hamburg, Germany), a member of the Helmholtz Association HGF, for the provision of experimental facilities. Parts of this research were conducted at PETRA III, and we would like to thank Azat Khadiev for assistance in using P23. Beamtime was allocated for proposal I-20231380 EC. Rik Vaerenberg would like to acknowledge the FWO SBO fellowship program (project number: 1SE9325N), the FWO Travel grant (grant number: V445325N) and the support of Flanders Make, the strategic research center for the manufacturing industry via the MUSIC SBO project. The authors would also like to thank Dr. R. Richter for his technical support, and Prof. P. Hoffmann for his helpful and fruitful discussions.

Appendix A. Supplementary data

Supplementary data to this article can be found online at https://doi.org/10.1016/j.optlastec.2025.114591.

Data availability

Data will be made available on request.

References

[1] J. Humphreys, G. Rohrer and A. Rollett, Recrystallzation and Related Annealing Phenomena, Elsevier, 2017.
[2] D. Raabe, "Recovery and Recrystallization: Phenomena, Physics, Models, Simulation," in Physical Metallurgy (Fifth Edition), Oxford, Elsevier, 2014, pp. 2291-2397. Doi: 10.1016/B978-0-444-53770-6.00023-X.
[3] A. Singh, S. Sharma, A. Batish, Dynamic recrystallization during solid state friction stir welding/processing/additive manufacturing: Mechanisms, microstructure evolution, characterization, modeling techniques and challenges, Critical Reviews in Solid State and Materials Science 50 (2025) 77–135, https://doi.org/10.1080/10408436.2024.2391333.
[4] P. Karimi, E. Sadeghi, J. Ålgårdh, A. Keshavarzkermani, R. Esmaeilizadeh, E. Toyserkani, J. Andersson, Columnar-to-equiaxed grain transition in powder bed fusion via mimicking casting solidification and promoting in situ recrystallization, Addit. Manuf. 46 (2021) 102086, https://doi.org/10.1016/j.addma.2021.102086.
[5] Z. Zou, M. Simonelli, J. Katrib, G. Dimitrakis, and R. Hauge. "Refinement of the grain structure of additive manufactured titanium alloys via epitaxial recrystallization enabled by rapid heat treatment," no. 180, pp. 66-70, 2020. Doi: 10.1016/j.scriptamat.2020.01.027.
[6] F. Yan, W. Xiong, E. Faierson, Grain Structure Control of Additively Manufactured Metallic Materials, Materials no. 10 (2017) 1260, https://doi.org/10.3390/ma10111260.
[7] P. Collins, D. Brice, P. Samimi, I. GHamarian and H. Fraser, "Microstructural Control of Additively Manufactured Metallic Materials," Annual Review of Materials Research, no. 46, pp. 63-91, 2016. Doi: 10.1146/annurev-matsci-070115-03181.
[8] K. Huang, R. Loge, A review of dynamic recrystallization phenomena in metallic materials, Mater. Des. 111 (2016) 548–574, https://doi.org/10.1016/j.matdes.2016.09.012.
[9] M. Buttard, B. Chehab, R. Shahani, F. Robaut, G. Renou, C. Tassin, E. Rauch, P. Donnadieu, A. Deschamps, J.-J. Blandin, G. Martin, Multi-scale microstuctural investigation of a new Al-Mn-Ni-Cu-Zr aluminium alloy processed by laser powder bed fusion, Materialia 18 (2021) 101160, https://doi.org/10.1016/j.mtla.2021.101160.
[10] E. Rauch, M. Veron, Automated crystal orientation and phase mapping in TEM, Mater Charact 98 (2014) 1–9, https://doi.org/10.1016/j.matchar.2014.08.010.
[11] S. Brandstetter, P. Derlet, S. Van Petegem, H. Van Swygenhoven, Williamson–Hall anisotropy in nanocrystalline metals: X-ray diffraction experiments and atomistic simulations, Acta Mater. 56 (2) (2008) 165–176, https://doi.org/10.1016/j.actamat.2007.09.007.
[12] A. Borbely, J. Driver, Dislocation density measurements by x-ray profile analysis in texture components of deformed metals, Arch. Metall. Mater. 50 (2005) 65–76.
[13] S. Hocine, H. Van Swygenhoven, S. Van Petegem, C. Chang, T. Maimaitiyili, G. Tinti, D. Sanchez, D. Grolimund, N. Casati, Operando X-ray diffraction during laser 3D printing, Mater. Today 34 (2020) 30–40, https://doi.org/10.1016/j.mattod.2019.10.001.
[14] C. Navarre, S. Van Petegem, L. Schlenger, C. Cayron, M. Hamidi-Nasab, R. Esmaeilzadeh, C. de Formanoir, N. Casati, R. Loge, Monitoring of laser-induced fast recrystallization in SS-316L through synchrotron X-ray diffraction, Mater. Des. 238 (2024) 112628, https://doi.org/10.1016/j.matdes.2023.112628.
[15] V. Pandiyan, G. Masinelli, C. Navarre, T. Le-Quang, M. Hamidi-Nasab, C. de Formanoir, R. Esmaeilzadeh, S. Goel, F. Marone, R. Loge, S. Van Petegem, K. Wasmer, Deep learning-based monitoring of laser powder bed fusion process on variable time-scales using heterogeneous sensing and operando X-ray radiography guidance, Addit. Manuf. 58 (2022) 103007, https://doi.org/10.1016/j.addma.2022.103007.
[16] E. Lindh-Ulmgren, M. Ericsson, D. Artymowicz, W. Hutchinson, Laser-Ultrasonics as a Technique to Study Recrystallisation and grain growth, Mater. Sci. Forum 467–470 (2004) 1353–1362, https://doi.org/10.4028/www.scientific.net/MSF.467-470.1353.
[17] M. Hossain, H. Taheri, In Situ Process monitoring for Additive Manufacturing through Acoustic Techniques, J. Mater. Eng. Perform. 29 (2020) 6249–6262, https://doi.org/10.1007/s11665-020-05125-w.
[18] V. Pandiyan, R. Drissi-Daoudi, S. Shevchik, G. Masinelli, R. Loge, K. Wasmer, Analysis of time, frequency and time-frequency domain features from acoustic emissions during Laser Powder-Bed fusion process, Procedia CIRP 94 (2020) 392–397, https://doi.org/10.1016/j.procir.2020.09.152.
[19] V. Pandiyan, R. Drissi-Daoudi, S. Shevchik, G. Masinelli, T. Le-Quang, R. Loge, K. Wasmer, Semi-supervised monitoring of Laser powder bed fusion process based on acoustic emissions, Virtual and Physical Prototyping 16 (4) (2021) 481–497, https://doi.org/10.1080/17452759.2021.1966166.
[20] C. Scruby, C. Jones, J. Titchmarsh, H. Wadley, Relationship between microstructure and acoustic emission in Mn-Mo-Ni A533B steel, Metal Science 15 (6) (1981) 241–261, https://doi.org/10.1179/030634581790426750.
[21] W. Schaarwachter, H. Ebener, Acoustic emission: a probe into dislocation dynamics in plasticity, Acta Metall. Mater. 38 (2) (1990) 195–205, https://doi.org/10.1016/0956-7151(90)90049-M.
[22] J. Frederick, D. Felbeck, "Dislocation Motion As a source of Acoustic Emission," in Acoustic Emission, ASTM International (1972) 129–139, https://doi.org/10.1520/STP35385S.
[23] Y. Chen, K. Tang, B. Gou, F. Jiang, X. Ding, E. Salje, Acoustic emission spectra and statistics of dislocation movements in Fe40Mn40Co10Cr10 high entropy alloys, J. Appl. Phys. 132 (8) (2022) 080901, https://doi.org/10.1063/5.0098813.
[24] Y. Chen, B. Gou, B. Yuan, X. Ding, J. Sun and E. Salje, "Multiple Avalanche Processes in Acoustic Emission Spectroscopy: Multibranching of the

Energy−Amplitude Scaling," physica status solidi (b), vol. 259, no. 3, p. 2100465, 2021. Doi: 10.1002/pssb.202100465.
[25] Y. Chen, B. Gou, W. Fu, C. Chen, X. Ding, J. Sun, E. Salje, Fine structures of acoustic emission spectra: how to separate dislocation movements and entanglements in 316L stainless steel, Appl. Phys. Lett. 117 (26) (2020) 262901, https://doi.org/10.1063/5.0030508.
[26] L. Chen, Y. Huang, W. Li, R. Yang, X. Chen, G. Zhang, Y. Rong, Acoustic emission monitoring and heat-affected zone evaluation of CFRP laser cutting, Compos. Struct. 304 (2023) 116419, https://doi.org/10.1016/j.compstruct.2022.116419.
[27] S. Shu, Y. He, L. Chen, W. He, L. Zhou, X. Pan, S. Xuan, Y. Rong, W. Li, High-quality drilling method for CFRP blind holes guided by acoustic emission signals, Mech. Syst. Sig. Process. 224 (2025) 112029, https://doi.org/10.1016/j.ymssp.2024.112029.
[28] R. Esmaeilzadeh, V. Pandiyan, S. Van Petegem, M. Van der Meer, M. Nasab, C. de Formanoir, J. Jhabvala, C. Navarre, L. Schlenger, R. Richter, N. Casati, K. Wasmer, R. Loge, Acoustic emission signature of martensitic transformation in laser powder bed fusion of Ti6Al4V-Fe, supported by operando X-ray diffraction, Addit. Manuf. 96 (2024) 104562, https://doi.org/10.1016/j.addma.2024.104562.
[29] S. Hocine, S. Van Petegem, U. Frommherz, G. Tinti, N. Casati, D. Grolimund, H. Van Swygenhoven, A miniaturized selective laser melting device for operando X-ray diffraction studies, Addit. Manuf. 34 (2020) 101194, https://doi.org/10.1016/j.addma.2020.101194.
[30] C. de Farmanoir, M. Hamidi Nasab, L. Schlenger, S. Van Petegem, G. Masinelli, F. Marone, A. Salminen, A. Ganvir, K. Wasmer, R. Loge, Healing of keyhole porosity by means of defocused laser beam remelting: Operando observation by X-ray imaging and acoustic emission-based detection, Addit. Manuf. 79 (2024) 103880, https://doi.org/10.1016/j.addma.2023.103880.
[31] M. Hamidi Nasab, G. Masinelli, C. de Farmanoir, L. Schlenger, S. Van Petegem, R. Esmaeilzadeh, K. Wasmer, A. Ganvir, A. Salminen, F. Aymanns, F. Marone, V. Pandiyan, S. Goel, R. Loge, Harmonizing sound and light: X-ray imaging unveils acoustic signatures of stochastic inter-regime instabilities during laser melting, Nat. Commun. 14 (1) (2023) 8008, https://doi.org/10.1038/s41467-023-43371-3.
[32] H. Ghasemi-Tabasi, J. Jhabvala, E. Boillat, T. Ivas, R. Drissi-Daoudi, R. Loge, An effective rule for translating optimal selective laser melting processing parameters from one material to another, Addit. Manuf. 36 (2020) 101496, https://doi.org/10.1016/j.addma.2020.101496.
[33] G. Ashiotis, A. Deschildre, Z. Nawaz, J. Wright, D.P.F. Karkoulis, The fast azimuthal integration Python library: PyFAI, J. Appl. Cryst. 48 (2015) 510–519, https://doi.org/10.1107/S1600576715004306.
[34] J. Lv, J.-H. Zheng, V. Yardley, Z. Shi, J. Lin, A Review of Microstructural Evolution and Modelling of Aluminium Alloys under Hot Forming Conditions, Metals 10 (11) (2020) 1516, https://doi.org/10.3390/met10111516.
[35] P. Desai and C. Ho, "Thermal Linear Expansion of Nine Selected AISI Stainless Steels," American Iron and Steel Institute, 1978.
[36] R. Jenkins and R. Snyder, "Introduction to X-Ray Powder Diffractometry", John Wiley & Sons Inc., 1996.
[37] J. Revathy, N. Chitra Priya, K. Sandhya, D. Rajendran, Structural and optical studies of cerium doped gadolinium oxide phosphor, Bull. Mater. Sci. 44 (2021) 13, https://doi.org/10.1007/s12034-020-02299-w.
[38] P. Scheel, P. Markovic, S. Van Petegem, M. Makowska, R. Wrobel, T. Mayer, C. Leinenbach, E. Mazza, E. Hosseini, A close look at temperature profiles during laser powder bed fusion using operando X-ray diffraction and finite element simulations, Addit. Manuf. Lett. 6 (2023) 100150, https://doi.org/10.1016/j.addlet.2023.100150.
[39] A. Jerri, The Shannon sampling theorem—Its various extensions and applications: a tutorial review, Proc. IEEE 65 (11) (1977) 1565–1596, https://doi.org/10.1109/PROC.1977.10771.
[40] I. Roy, P. Ray, G. Balasubramanian, Modeling Oxidation of AlCoCrFeNi High-Entropy Alloy using Stochastic Cellular Automata, Entropy 24 (9) (2022) 1263, https://doi.org/10.3390/e24091263.
[41] D. Bergstrom, The Absorptance of Metallic Alloys to Nd: YAG and Nd: YLF Laser Light, Lulea University of Technology, 2005.
[42] R. Drissi-Daoudi, V. Pandiyan, R. Loge, S. Shevchik, G. Masinelli, H. Ghasemi-Tabasi, A. Parrilli, K. Wasmer, Differentiation of materials and laser powder bed fusion processing regimes from airborne acoustic emission combined with machine learning, Virtual and Physical Prototyping (2022) 181–204, https://doi.org/10.1080/17452759.2022.2028380.
[43] P. Welch, "The use of fast Fourier transform for the estimation of power spectra: A method based on time averaging over short, modified periodograms," IEEE Transactions on Audio and Electroacoustics, vol. 15, no. 2, 1967. Doi: 10.1109/TAU.1967.1161901.
[44] V. Pandiyan, R. Wrobel, C. Leinenbach, S. Shevchik, Optimizing in-situ monitoring for laser powder bed fusion process: Deciphering acoustic emission and sensor sensitivity with explainable machine learning, J. Mater. Process. Technol. 321 (2023) 118144, https://doi.org/10.1016/j.jmatprotec.2023.118144.